



Cite this: *Green Chem.*, 2023, **25**, 6748

Scalable nitrogen-enriched porous sub-100 nm graphitic carbon nanocapsules for efficient oxygen reduction reaction in different media†

Kamel Eid, ^a Ali A. Abdelhafiz, ^b Safwat Abdel-Azeim, ^c Rajender S. Varma ^d and Mohamed F. Shibl^e

The oxygen reduction reaction (ORR) is deemed a sustainable energy source; however, developing green, earth-abundant, and efficient noble-metal-free catalysts for efficient ORR in different media remains a grand challenge. Herein, we present a scalable, facile, environmentally benign, and one-pot strategy for the fabrication of eco-friendly nitrogen-enriched graphitic-like hierarchical porous sub-100 nm carbon (denoted as N-HMPC) nanocapsules with controllable N-content for ORR. The synthesis route is based on *in situ* organic-organic self-assembly of Pluronic F127 copolymer micelles and resorcinol–melamine–formaldehyde in the presence of a silica template followed by carbonization and eroding the silica core. The as-formed N-HMPC nanocapsules have a core–shell morphology (~84 nm), hierarchical porosity, high surface area of (790 m² g^{−1}), and tunable nitrogen content (9–25%). Intriguingly, N-HMPC nanocapsules exhibit an analogous ORR activity to the commercial Pt/C catalyst (20% Pt) in the alkaline and acidic electrolytes, besides superior durability and inimitable tolerance to methanol and CO poisonings due to the hollow core–shell architecture and abundant nitrogen. A judicious combination of experimental and density functional theory (DFT) simulations delineated the ORR pathway and mechanism for N-HMPC in acidic and alkaline electrolytes. The presented approach may open new avenues for the rational design of metal-free green electrocatalysts for ORR.

Received 25th May 2023,
Accepted 22nd June 2023
DOI: 10.1039/d3gc01790g

rsc.li/greenchem

Introduction

Proton exchange membrane fuel cells (PEMFCs) are environmentally friendly and possess higher energy density and faster refueling due to their outstanding energy density and zero emissions.^{1,2} Nevertheless, the commercialization of PEMFCs is still impractical due to the intolerable cost associated with expensive catalyst component (*i.e.*, Pt) at the cathode side to mitigate the sluggish oxygen reduction reaction (ORR).^{3,4}

Enormous efforts have been made to optimize catalyst performance to achieve better material utilization at significantly lower costs. Potential solutions have culminated in the enhancement of mass activity, controlling particle size,^{3–5} morphology, and composition of Pt-based catalyst with its metal group.^{6–9} Other strategies included the replacement of Pt with non-precious metals/metal oxides or mixing with carbon-based nanostructured electrocatalysts.^{10–12} Porous carbon nanostructures are promising green candidates for ORR due to their low cost, high electrical conductivity, unique chemical, thermal stabilities, and large surface area.^{13,14} Also, they can easily be prepared from eco-friendly and inexpensive earth-abundant materials without environmental risks. Notably, the electrocatalytic activity of porous carbon-based nanostructures remains out of the practical application demand owing to their hydrophobicity and limited catalytic active sites.¹⁴

Integration of heteroatom dopants (*e.g.*, P, S, and N) or metal atoms (*e.g.*, Fe, Co, and Cu) into the carbon matrix tune their physicochemical properties, which produce charged defective sites with high adsorption affinity to O₂, along with an inferior energy barrier for adsorption of ORR intermediates.^{15–17} Remarkably, nitrogen heteroatom doping alters the crystal structures and electronic configuration of carbon catalyst substantially, compared to other heteroatom

^aGas Processing Center (GPC), College of Engineering, Qatar University, Doha 2713, Qatar. E-mail: kamel.eid@qu.edu.qa

^bDepartment of Nuclear Science Engineering, Massachusetts Institute of Technology, Cambridge, MA 02139, USA. E-mail: ali_m@mit.edu

^cCenter for Integrative Petroleum Research (CIPR), College of Petroleum Engineering and Geosciences, King Fahd University of Petroleum and Minerals (KFUPM), Dhahran 31261, Saudi Arabia

^dRegional Centre of Advanced Technologies and Materials, Czech Advanced Technology and Research Institute, Palacky University, Slechitellu 27, 783 71 Olomouc, Czech Republic. E-mail: varma.rajender@epa.gov

^eCenter for Sustainable Development, College of Arts and Sciences, Qatar University, Doha 2713, Qatar

†Electronic supplementary information (ESI) available: Experimental section, TEM, Raman, EDX, XPS, cyclic voltammogram, and DFT simulation. See DOI: <https://doi.org/10.1039/d3gc01790g>



dopants.^{14,18} This is in addition to enhancing chemical stability, surface polarity, and electric conductivity of carbon catalyst, which are beneficial for promoting ORR electrocatalytic activity.^{14,18,19} Nitrogen, as an electron-rich atom, introduces an abundance of no-pair electrons, which facilitates the formation of positive charges on its adjacent carbon neighbors, forming the N^--C^+ dipole.^{14,18–21} This, in consequence, tailors the atomistic charge distribution of carbon, maximizing the utilization of π -electrons, accelerating the ORR kinetics, and providing a high tolerance for poisons.^{14,18–21} For instance, a variety of N-doped carbon nanostructures have displayed an enhanced ORR activity and poison-tolerance superior to Pt-carbon (Pt/C) catalyst.^{22–29}

Significant efforts have been devoted to the fabrication of N-enriched porous carbon-based nanostructures with various morphologies, including but not limited to nanosheets, nanospheres, polyhedrals, nanotubes, and nanofibers for various catalytic reactions.^{30–32} Nevertheless, most of the nanostructures mentioned above revealed dominant tortuous micropores or mesopores with a low nitrogen content (7–14%), which are less beneficial to diffusion or adsorption of ORR reaction intermediates.^{30–34} Moreover, the rational green synthesis of N-enriched sub-100 nm carbon nanostructures with multiple pores, high surface area, and tunable nitrogen content for ORR is not hitherto addressed. Meanwhile, the effect of N-content on ORR performance has not been reported. Tailoring the formation of N-enriched-sub-100 nm carbon nanocapsules with various pores is envisioned to enhance ORR performance significantly.

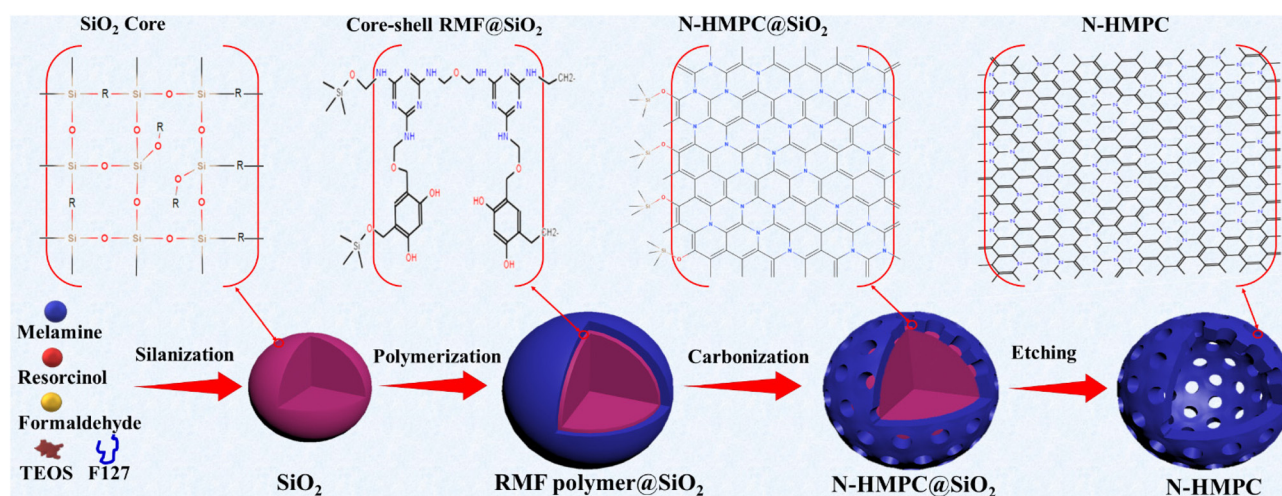
Herein, we report a facile, scalable, and green approach for the scalable design of N-enriched graphitic-like porous carbon (N-HMPC) nanocapsules from eco-friendly, cheap, and earth-abundant materials. The synthesis protocol is based on the *in situ* formation of a thin layer of resorcinol–melamine–formaldehyde (RMF) coated on a silica core, followed by carbonization and etching of the silica core. The adjustment of the

hydrophilic–hydrophobic balance of the reaction medium allows efficient consecutive organic–organic self-assembly of Pluronic micelles and RMF, coating the silica nanoparticles. Compared to other reports, the presented approach is straightforward, greener, cost-effective, sustainable, and suitable for mass production of uniformly dispersed sub-100 nm N-HMPC with ordered porosity (micropores, mesopores, and macropores), high surface area ($790\text{ m}^2\text{ g}^{-1}$), and tunable nitrogen content (9–25%). Also the discharge of N-HMPC to the environment will not cause any hazardous effects because it contains only carbon and nitrogen. The abundant disparate pores can function as accommodation sites for reactants and/or ion-transport paths, which enhances the electrolyte permeability and accelerates mass transport. The ORR performance of N-HMPC nanocapsules was investigated relative to nitrogen-free HMPC and commercial Pt/C catalyst in both alkaline and acidic media, in addition to investigating the effect of N-content on the ORR. Moreover, ORR pathways were investigated experimentally and theoretically using the DFT simulations to unravel the ORR mechanism on N-HMPC.

Results and discussion

Characterization and properties

Scheme 1 shows the green formation process and proposed mechanism of nitrogen-enriched hollow mesoporous carbon nanocapsules (N-HMPC) from inexpensive and earth-abundant materials. This includes melamine, TEOS, resorcinol, formaldehyde, and KOH, which are recoverable as byproducts of different industrial processes and also could be obtained using green methods to meet sustainability needs. This included the one-step formation of a thin layer of resorcinol–melamine–formaldehyde (RMF) wrapped silica core, followed by consecutive carbonization and eroding the silica core (Scheme 1). Fig. S1a† shows the low-magnification TEM image



Scheme 1 Fabrication process and proposed formation mechanism of N-HMPC beside its related chemical structures and 3D model.



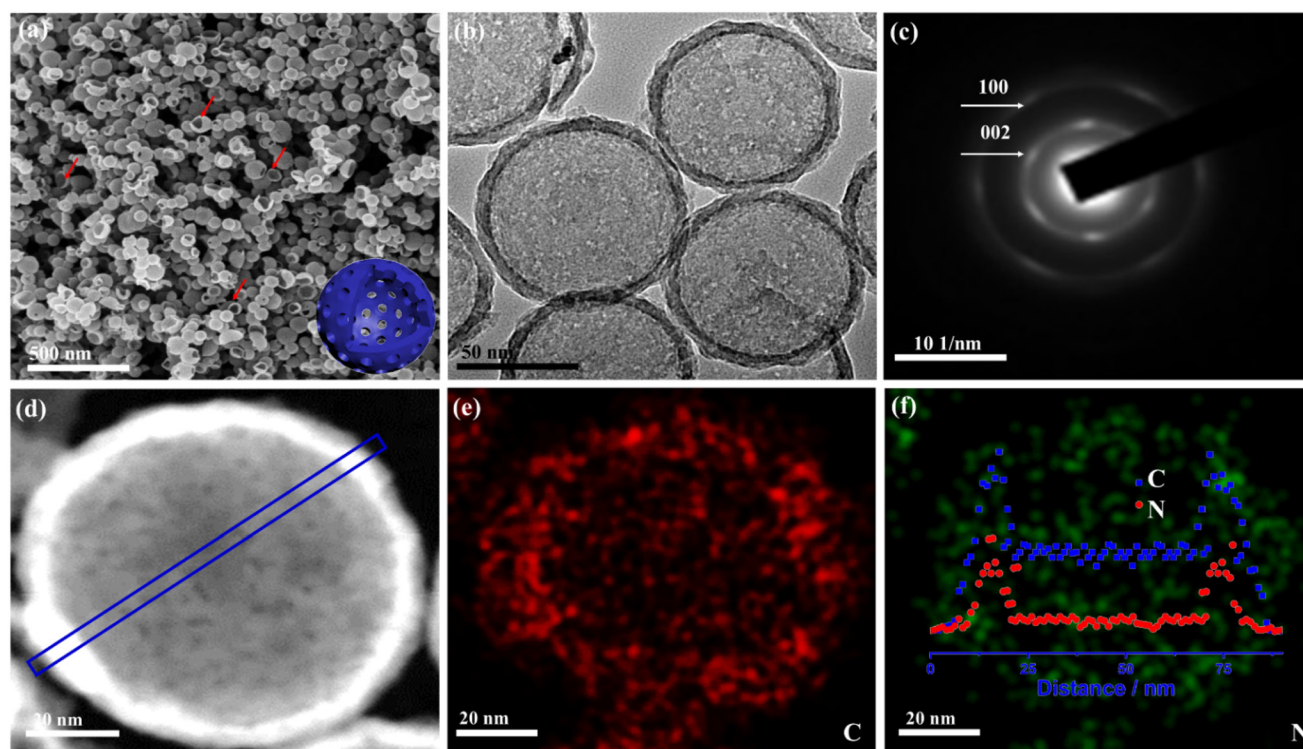


Fig. 1 (a) SEM, (b) TEM image, and (c) SAED of N-HMPC. (d) HAADF-STEM of N-HMPC and its elemental mapping for (e) carbon and (f) nitrogen. The inset in (f) shows a cross-section composition line profile for the marked area in (e).

of N-HMPC@SiO₂ obtained in a high yield of uniform nanospheres with a well-defined core-shell structure. After the selective erosion of the SiO₂ core by dilute KOH solution in hot water solution, N-HMPC was formed in a well-defined capsule-like structure with a spherical shape and open pore as indicated by the arrows (Fig. 1a), and the average diameter of the ensued N-HMPC being 85 ± 3 nm (Fig. S1b†). The TEM confirmed that N-HMPC comprises a carbon shell with an average thickness of 12 nm and a large macropore of ~ 72 nm with various mesopores (Fig. 1b).

The selected area electron diffraction pattern (SAED) resolved the typical diffraction ring assigned to the {002} and {100} facets of graphitic-like carbon nanostructure (Fig. 1c).²⁴ The EDX displayed only the presence of C and N with atomic contents of 75.7 and 24.3%, respectively, which implied the formation of nitrogen-enriched carbon structures (Fig. S1c†). This originated from the polymerization and condensation of melamine (containing 65% nitrogen) with resorcinol and formaldehyde in agreement with the previous report.³⁵

The HAADF-STEM image also demonstrated the formation of hierarchical hollow core-shell nanocapsules decorated with multiple pores (Fig. 1d). The elemental mapping analysis revealed the homogenous distribution of C and N atoms in the as-formed N-HMPC (Fig. 1e and f). The cross-sectional compositional line profile revealed the formation of a core-shell structure (inset in Fig. 1f) with a coherent atomic content of 74.7 and 25.3 for C and N, respectively, which is close to the

EDX analysis. Nitrogen-free HMPC was synthesized by the same method as N-HMPC but without melamine.

The TEM images of the HMPC@SiO₂ nanostructure showed its high-yield formation of core-shell structures (Fig. S1d and e†). After the removal of the SiO₂ core, HMPC porous structure was obtained with an average diameter of 80 ± 3 nm and a shell thickness of 7 nm (Fig. S1f†). The outer layer of the N-HMPC area presented a graphitic-like nanostructure with multiple graphitic layers with an average interlayer spacing of 3 nm, as affirmed by high-resolution TEM (HRTEM) (Fig. 2a and b). Meanwhile, the sub-graphitic layer was highly amorphous.

The fast-Fourier-transform (FFT) of the outer layer displays multiple graphitic layer structures (Fig. 2c). These structures have multiple repeated well-aligned layers with significant twists, distortions, and defects, as indicated by the arrows in (Fig. 2d), owing to the high nitrogen content, corroborating earlier reports.³⁵ This implies that the outer graphitic edges in the N-HMPC are defect-rich, which plausibly offers an abundance of reactive sites for ORR.³⁷ The spacing between adjacent graphite planes varied from 0.3 to 0.45 nm, close to the *d*-spacing of (002) crystal plane (0.335 nm) of bulk graphite (Fig. 2e–h), which implies the high crystallinity of the graphitic layers. hexagonal carbon rings (Fig. 2c), as generally reported for N-enriched porous carbon materials.^{35,36}

This verifies the transformation of the polymeric RMF into a graphitic-like carbon nanostructure after pyrolysis at elevated



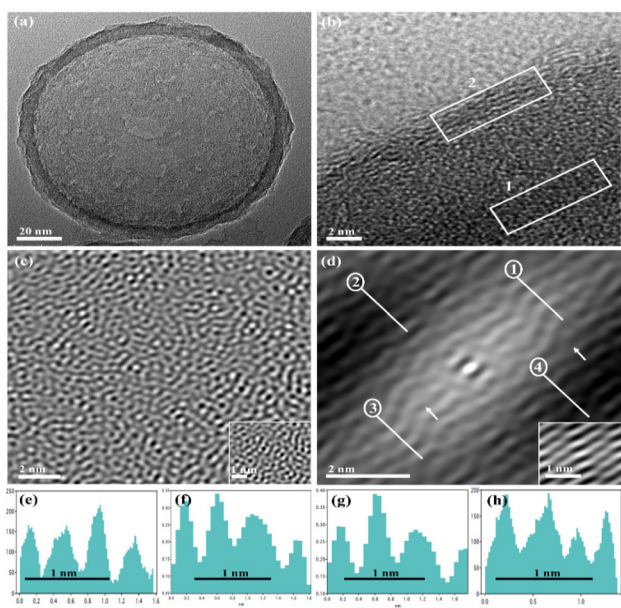


Fig. 2 (a) High magnification TEM of a single N-HMPC nanocapsule, (b) HRTEM image of the shell area. (c) FFT of the marked area (1b). (d) FFT of marked area (2b). (e–h) Histograms obtained from the digital micrograph showing the lattice spacing of graphitic layers (d1–d4, respectively).

temperatures. Fast Fourier transformed HRTEM (FFT-HRTEM) image analysis of the amorphous core, after silica etching, confirmed the arrangement of carbon atoms in a honeycomb-like structure, along with various distortions after etching of SiO_2 core.

Fig. 3a displays the XRD spectra of as-prepared N-HMPC and HMPC, wherein both have a sharp diffraction peak at

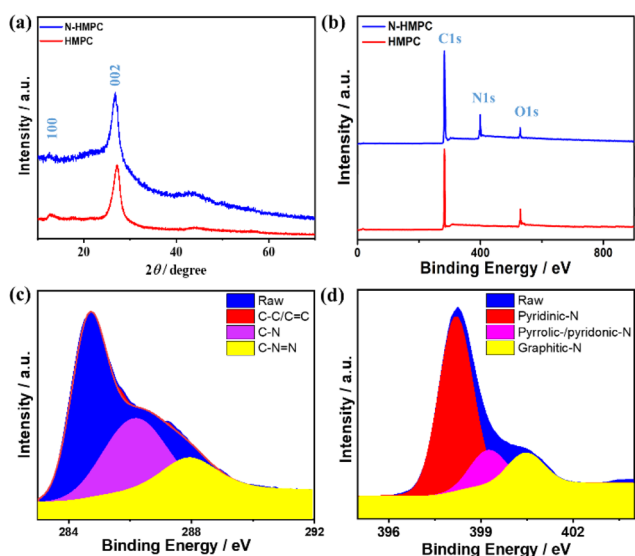


Fig. 3 (a) Wide-angle XRD spectra of typically synthesized N-HMPC and HMPC. (b) XPS-survey spectra of N-HMPC and HMPC. (c) High-resolution XPS spectrum of C. (d) High-resolution XPS spectrum of N.

27.3° corresponding to the (002) facet and small plateau at 13° attributed to the (100) facet resulting from the interplanar stacking of the conjugated aromatic segment of the graphitic-like carbon structure.⁴⁵ The diffraction peaks of N-HMPC were more intense and slightly shifted to a lower angle relative to HMPC, resulting from the high nitrogen content and the presence of a high density of nanopores.³⁵ The absence of any foreign diffraction peaks inferred the purity of the formed carbon nanostructures, with completed carbonization after annealing at elevated temperatures.

The XPS survey scans of N-HMPC and HMPC samples showed photoemissions of C 1s with some minor O 1s species, while on the other hand, N-HMPC exclusively showed the presence of N 1s (Fig. 3b). The near-surface composition determined by XPS indicated that the atomic contents of C and N in N-HMPC were 75.1 and 24.9%, respectively, which matched the elemental mapping results obtained from the EDX analysis discussed earlier.

High-resolution scans of C 1s spectra of N-HMPC revealed the existence of sp^2 graphitic carbon (C–C/C=C) at 284.9 eV, sp^3 -hybridized carbon bonded to nitrogen (C–N) at 286.3 eV, and sp^2 carbon–nitrogen of the aromatic rings (N–C=N) at 288.1 eV (Fig. 3c). Likewise, N 1s spectra showed three peaks assigned to pyridinic-N (398.6 eV), pyrrolic/pyridonic-N (400.1 eV), and graphitic-N (401.7 eV) as the main features for nitrogen-enriched carbon structure (Fig. 3d).³⁵ The EDX and XPS data confirmed the existence of significant nitrogen content within the bulk and at the surface of N-HMPC. The presence of these nitrogen states is expected to influence the charge density on the adjacent carbon atoms and create various defective active sites, which can subsequently exhibit distinct ORR activity.^{14,35}

The Raman spectra of both N-HMPC and HMPC showed typical D and G bands at 1346.7 and 1545.8 cm^{-1} , respectively (Fig. S2†). In addition, the exclusive presence of the G' band ($\sim 2620\text{ cm}^{-1}$) for N-HMPC was attributed to the disordered and defective carbon. The I_D/I_G of N-HMPC was calculated to be 1.2, compared to I_D/I_G of 1.04 for HMPC, which additionally implies the higher defective nature of N-HMPC.^{38,39} Highly defective carbon is well known for the improvement of the electrical conductivity and charge transfer during electrocatalytic reactions.³⁵

Fig. 4a and c depict the N_2 adsorption isotherms of N-HMPC and HMPC, respectively, where both exhibited closer isotherm behaviour to the type IV curve with an H4 hysteresis loop. The surface areas of N-HMPC and HMPC determined using a Brunauer–Emmett–Teller (BET) were 790 and $350\text{ m}^2\text{ g}^{-1}$, respectively. The higher surface area of N-HMPC, compared to HMPC, was attributed to the large porosity, which can be inferred from the larger hysteresis loop at $0.45 < P/P_0 < 0.9$. N-HMPC showed multiple bimodal pore-size distributions in the micro-, meso-, and microporous areas, which was shown by two-step capillary condensation in the range of $P/P_0 < 0.1$ and $P/P_0 > 0.9$ (Fig. 4b).⁴⁰ The pore volume of N-HMPC, determined by the Barrett–Joyner–Halenda method, was two folds higher than that of HMPC (Fig. 4d) because of the addition of



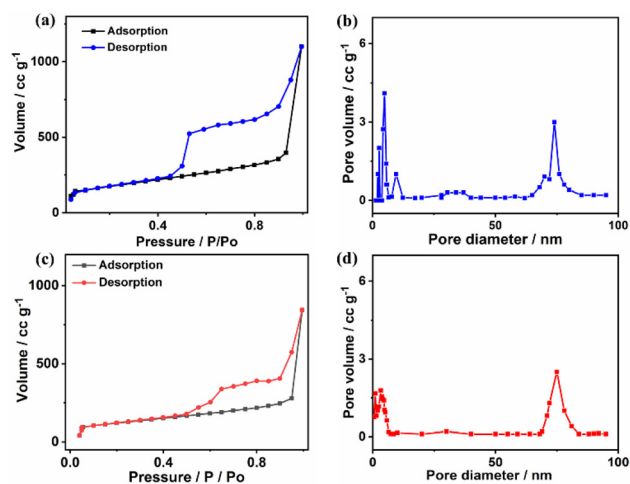


Fig. 4 N_2 adsorption–desorption isotherms and pore-size distributions of N-HMPC (a and b). N_2 adsorption–desorption isotherms and pore-size distributions of HMPC (c and d).

melamine, which contains significant nitrogen content that plausibly releases N-based gases during the annealing process.⁴⁰

Optimization of N-HMPC and formation mechanism

Various reaction experiments were performed to optimize the structural understanding of the fabrication mechanism for N-HMPC. The sequence of reactant addition was observed to be a crucial factor, as a coating of SiO_2 by carbon shell under the Stöber method conditions is extremely difficult in one step. A critical step in the presented synthesis herein was the initial mixing of NH_4OH with ethanol and water for 30 min before the addition of the remaining reagents. Contrarily, adding TEOS to ethanol and water before adding NH_4OH resulted in particle aggregation (Fig. S3a†). The initial addition of NH_4OH before TEOS decorates the colloidal SiO_2 with NH_4^+ ions under basic conditions, which prevents the agglomeration of the resultant SiO_2 nanoparticles and provides a strong electrostatic interaction with hydroxymethyl-substituted species derived from the polymerization and condensation of resorcinol–melamine–formaldehyde. The quick addition of NH_4OH and TEOS produced aggregated particles (Fig. S3b†). Hollow N-HMPC without mesopore core is formed without Pluronic F127 (Fig. S3c†). Increasing the concentration of Pluronic F127 to 0.2 g resulted in the formation of N-HMPC with bigger mesopores within the particle's core, indicating the significant role of Pluronic F127 as a pore modulator (Fig. S3d†). The influence of Pluronic F127 is believed to be a result of hydrogen-bond formation between hydroxyl groups in Pluronic F127 and the solvent, producing micelles assembled with one-another into a porous structure. Decreasing the concentration of Pluronic F127 to 0.05 g produced nanocapsules with distorted and irregular pores (Fig. S3e†). The etching of SiO_2 in KOH (15 wt%) destroyed the nanocapsules (Fig. S3f†). The N-content and the carbon-shell thickness could be fine-

tuned by adjusting the concentration of melamine (Fig. S4†). N-HMPC-1 and N-HMPC-2 with a shell thickness of 5 nm (Fig. S4a†) and 8 nm (Fig. S4b†) are synthesized by using 0.04 and 0.09 g of melamine, respectively. Both samples had a lower thickness relative to the typical sample prepared using 0.13 g of melamine (N-HMPC-3) (Fig. S4c†). The XPS scan analysis revealed that the N-content was 9.5, 14.3, and 24.9% for N-HMPC-1, N-HMPC-2, and N-HMPC-3, respectively (Fig. S4d†).

The shape evolution of N-HMPC was investigated by collecting four samples at different reaction times and imaging them under TEM (Fig. S5†). Initially, spherical SiO_2 particles are formed with size in the range of 72 ± 3 nm within almost 1 h (Fig. S5a†). After 1.5 h of reaction, a thin shell (nearly 3 nm) of resorcinol–melamine–formaldehyde (RMF) was grown over the surface of SiO_2 particles (Fig. S5b†). The thin shell grew further and became thicker as the reaction time elapsed (Fig. S5c†). The polymerization process was slow as it required 5 h for it to be completed (Fig. S5d†). Notably, the formation of core–shell needs 24 h for completion when the reaction is conducted at room temperature. Therefore, the reaction temperature was increased to 50 °C to accelerate polymerization kinetics to form core–shell within 6 h. The morphological evolution of N-HMPC can be observed by the naked eye through color changes of the reaction solution from color-less to milky-white, then to yellowish, and finally to brown, which was attributed to the successive formation of SiO_2 core, growing carbon shell, and completing the polymerization/condensation of carbon-shell, correspondingly. Thus, the proposed formation mechanism for N-HMPC is attributed to the prompt formation of SiO_2 nanoparticles that complex with Pluronic F127 and forms small clusters that serve as nucleation sites for the adsorption melamine–resorcinol–formaldehyde (RMF) complex shell. Afterwards, the polymerization and condensation of RMF ensued a multi-layered polymeric network-like structure followed by carbonization at an elevated temperature, where melamine performed as C and N sources.^{40,41} Therefore, the self-assembly of Pluronic F127 micelles and RMF over silica produces multiple and abundant pores. Meanwhile, melamine in RMF yields a high nitrogen content.

Electrocatalytic activity in alkaline media

Inspired by the unique characteristics of N-HMPC nanocapsules, its catalytic performance was evaluated relative to HMPC and state-of-the-art Pt/C catalysts for ORR that are considered as a green energy source and also highly sensitive to structural and compositional merits of nanocatalyst. The CV curve of commercial Pt/C catalyst revealed typical voltammogram features, including three potential regions of the double-layered hydrogen waves ($H_{ads/des}$), formation of an OH_{ads} layer, and Pt_{Oxid}/Pt_{Red} (Fig. S6†). The CV scans of both N-HMPC and HMPC comprise a quasi-rectangular shaped voltammogram, typical for high-surface-area carbon catalysts, owing to their high capacitance (Fig. S6†). The capacitive current density of N-HMPC is significantly higher than that of HMPC and Pt/C catalyst due to its high conductivity and abundance of active



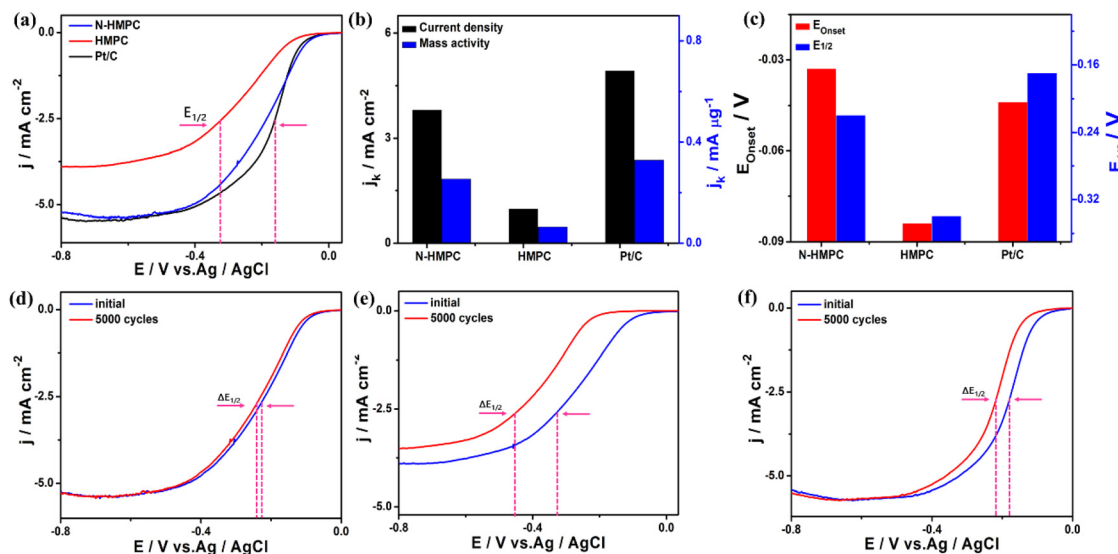


Fig. 5 (a) LSV curves of ORR catalyzed by different catalysts, (b) comparison of the measured current density and mass activities at -0.13 V, (c) comparisons of $E_{1/2}$ and E_{onset} . LSV for ORR durability of N-HMPC (d), HMPC (e), and Pt/C (f). LSV curves were measured in O_2 -saturated 0.1 M KOH solution at a scan rate of 20 mV s⁻¹, with 1600 rpm at room temperature.

catalytic sites. The ORR polarization curves measured in 0.1 M KOH at 20 mV s⁻¹ and 1600 rpm showed the diffusion-limited current (i_d) of N-HMPC (5.3 mA cm⁻²), which was comparable to that of Pt/C (5.44 mA cm⁻²), while HMPC showed a significantly lower current of 3.87 mA cm⁻² (Fig. 5a). The measured kinetic current (i_k) of N-HMPC, HMPC, and Pt/C was 3.8 , 0.97 , and 4.92 mA cm⁻², respectively (Fig. 5b).

The ORR mass activity of N-HMPC reached (0.25 mA μg⁻¹), which was found to be 75% of the Pt/C (0.33 mA μg⁻¹) and 3.9-folds of HMPC (0.064 mA μg⁻¹) (Fig. 5b). Enhancement of mass activity of N-HMPC over HMPC was attributed to the hollow nature and mesoporous structure of N-HMPC, providing a larger surface area, *i.e.*, an abundance of active sites, which promoted the adsorption of O_2 molecules. Doping of nitrogen in graphitic-like carbon heterocyclic ring can influence the spin density and charge distribution of neighbouring C-atoms, which creates more active sites and enhances mass transport and electron transfer.^{23,24} Interestingly, the onset potential (E_{onset}) of N-HMPC (-0.03 V) is substantially shifted

positively compared to Pt/C (-0.042) and HMPC (-0.084 V). Meanwhile, the half-wave potential ($E_{1/2}$) of N-HMPC (-0.19 V) was found to be close to that of Pt/C (-0.17 V), but significantly more positive than that of HMPC (-0.34 V) (Fig. 5c).

The catalytic performances of the vast majority of metal-free catalysts reported in the literature are usually lower than that of the commercial Pt/C catalyst in an alkaline medium.^{35,42–45} However, our results showed a competitive performance to state-of-the-art Pt/C. Moreover, the obtained ORR catalytic activity of our newly developed sub-100 nm N-HMPC nanocapsules was higher than previously reported N-doped porous carbon-based catalysts, such as Co-doped g-C₃N₄, N-P-doped C-porous foams, and other carbon structures, which have been evaluated under similar reaction conditions, as shown in Table 1.^{35,42–45}

Catalyst stability

The development of durable electrocatalysts for ORR is among the crucial barriers precluding the commercialization of ORR-

Table 1 ORR performance comparison showing the superior activity of presented N-HMPC herein relative to other N-enriched carbon structures presented elsewhere in the literature

Catalyst	BET Surface area (m ² g ⁻¹)	E_{onset} (V vs. Ag/AgCl)	$E_{1/2}$ (V vs. Ag/AgCl)	i_d (mA cm ⁻²)	Electron transfer number	Ref.
N-HMPC-3	790	-0.03	-0.19	5.44	3.9	This work
NGPC-1000-1	932	-0.02	-0.2	4.3	3.81	35
N-doped carbon nanotubes	280	-0.11	-0.23	3.5	2.7	42
N-doped Graphene	508	-0.03	-0.4	3.8	3.82	43
NPMC	1663	-0.04	-0.13	4.1	3.8	48
N-doped porous C	668	-0.12	-0.31	5.3	3	44
Porous Carbon-950	836	-0.06	-0.28	4.1	3.6	45
N-rGO	350	-0.15	-0.3	5.6	3.35	49
N,S,P doped carbon ring	378	-0.05	-0.22	2.8	3.7	50

fuel cells.^{3,46,47} Accelerated durability tests (ADT) were performed upon continuous potential cycles between 1.2–0.23 V for 5000 cycles in O₂-saturated 0.1 M KOH at a rotating speed of 1600 rpm with a scan rate of 20 mV s⁻¹. The *E*_{1/2} on N-HMPC degraded only by (0.02 V) (Fig. 5d), which was significantly lower than that on HMPC (0.1 V) (Fig. 5e) and Pt/C (0.04 V) (Fig. 5f). Thus, N-HMPC retained 90% of its *E*_{1/2}, which is highly stable compared to surviving 75% for Pt/C and 60% for HMPC (Fig. 5d–f). Interestingly, N-HMPC showed outstanding structural and morphological stability after ADT since the hollow mesoporous core-shell morphology of N-HMPC was fully intact compared to Pt/C, which suffered from aggregation and detachment of Pt (Fig. S7†).

The effect of nitrogen content on ORR performance was evaluated by testing three different samples with varying nitrogen contents of 9.5, 14.3, and 24.9%, labeled as N-HMPC-1, N-HMPC-2, and N-HMPC-3 (prepared under typical conditions), respectively, in O₂-saturated 0.1 M KOH (Fig. 6a). Intriguingly, the *I*_d (5.3 mA cm⁻²), *I*_k (3.8 mA cm⁻²), and *E*_{1/2} (−0.19 V) of N-HMPC-3 are substantially superior to its counterparts, which indicates that a higher content of N atom is preferred for enhancement of the ORR performance. Therefore, N-HMPC-3 is selected as an ideal catalyst platform for the rest of the remaining measurements.

Electrocatalytic activity in acidic media

It is often a challenge to design a versatile electrocatalyst that works effectively in different media.^{24,51–53} Therefore, the ORR performance of N-HMPC was evaluated relative to Pt/C catalyst and HMPC in O₂-saturated 0.5 M H₂SO₄ at 50 mV s⁻¹. Intriguingly, the obtained *I*_d of N-HMPC (4.1 mA cm⁻²) was

nearly 73.2% of Pt/C (5.6 mA cm⁻²) (Fig. 6b), whereas HMPC showed inferior activity. Additionally, at a current density of 2.8 mA cm⁻², the *E*_{1/2} of N-HMPC (0.71 V) was closer to that of the Pt/C catalyst (0.77 V). Meanwhile, the *E*_{onset} of N-HMPC was more positive relative to the Pt/C catalyst. The ORR ADT is performed upon continuous potential cycles from 0.2 V to 1 V for 5000 cycles in O₂-saturated 0.5 M H₂SO₄ at 1600 rpm at 20 mV s⁻¹. The *E*_{1/2} on N-HMPC degraded only by (0.03 V) (Fig. 6c), which was lower than that of Pt/C (0.055 V) (Fig. 6d), disclosing the tremendous stability of N-HMPC than Pt/C in H₂SO₄ electrolyte. The above analysis highlights the versatility of N-HMPC and the ability of nitrogen-enriched carbon-based materials to catalyze ORR in both acidic and basic media.^{24,51–53}

Fundamentals of ORR mechanism ORR pathways

The LSV curves were measured at various rotational speeds to explore the ORR kinetics of N-HMPC, H-MPC, and Pt/C in O₂-saturated 0.1 M KOH. The *I*_d of all catalysts increased steadily by increasing the rotational speed from 400 to 20 000 rpm (Fig. 7a, c, and e for N-HMPC, HMPC, and Pt/C, respectively). The Koutecky–Levich plots indicated excellent linearity on all catalysts with electron transfer numbers of 3.85, 2.5, and 3.92 on N-HMPC (Fig. 7b), HMPC (Fig. 7d) and Pt/C (Fig. 7f), respectively, at the potential range of −0.4 to −0.7 V. This demonstrated ORR kinetics with the four-electron pathway on N-HMPC and Pt/C, which is highly desirable to obtain maximum energy capacity with a high current density and avoiding the formation undesirable reaction products (*e.g.*, O₂^{•−}, O₂^{2−}, and H₂O₂). The LSV curves were measured at various rotational speeds to explore the ORR kinetics of N-HMPC catalysts in O₂-saturated 0.5 M H₂SO₄.

The *I*_d increased gradually with the increase in rotational speed from 400 to 20 000 rpm (Fig. 7g). The Koutecky–Levich plots indicated the linearity with electron transfer numbers of 3.7 to 3.9, respectively, at 0.5 to 0.8 V (Fig. 7h), implying its ORR kinetics with the four-electron pathway. Based on these findings, the ORR mechanism for N-HMPC may be explained by the ability of N-enriched carbon, with its electron properties, to create positively charged carbon atoms derived from the N[−]–C⁺ dipole, which is an active site for ORR (Scheme 2).^{14,18,19} N-HMPC allows the subsequent activation of O₂ molecules by direct bonding with the carbon atoms of nearby N-doped sites and prompt O–O dissociation under low potential. Meanwhile, the porous structure of N-HMPC is highly beneficial for quick mass transfer and electron mobility along with an excellent tolerance for reaction intermediates and products (Scheme 2).^{14,18,19} This is further supported by the DFT simulation.

DFT simulation

DFT simulation was carried out to unravel the ORR mechanism as well as the reaction pathways involving the different O-containing intermediates (*e.g.*, OOH*, O*, and OH*) over the typically synthesized N-HMPC compared to the metal-free HMPC in KOH and H₂SO₄ electrolytes. The DFT calculations

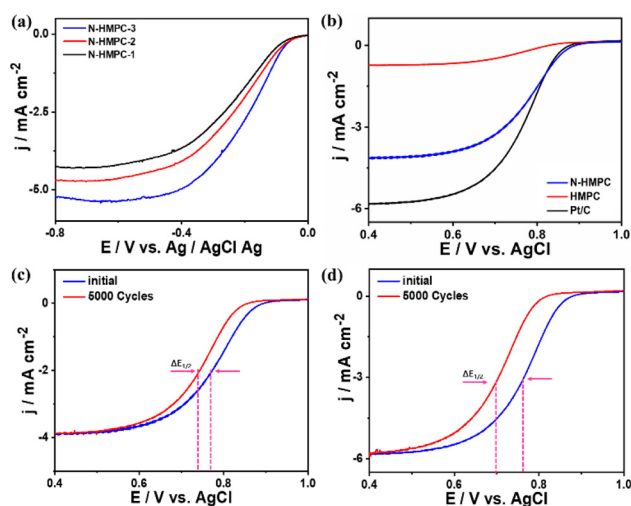


Fig. 6 (a) LSV for ORR measured in O₂-saturated 0.1 M KOH solution at a scan rate of 20 mV s⁻¹, with 1600 rpm on N-HMPC-3, N-HMPC-2, and N-HMPC-1. (b) LSV for ORR measured in O₂-saturated 0.5 M H₂SO₄ solution at a scan rate of 20 mV s⁻¹, with 1600 rpm. LSV for ORR durability measured in O₂-saturated 0.5 M H₂SO₄ solution at a scan rate of 20 mV s⁻¹, with 1600 rpm before and after 5000 cycles on (c) N-HMPC-3 and (d) Pt/C catalyst.



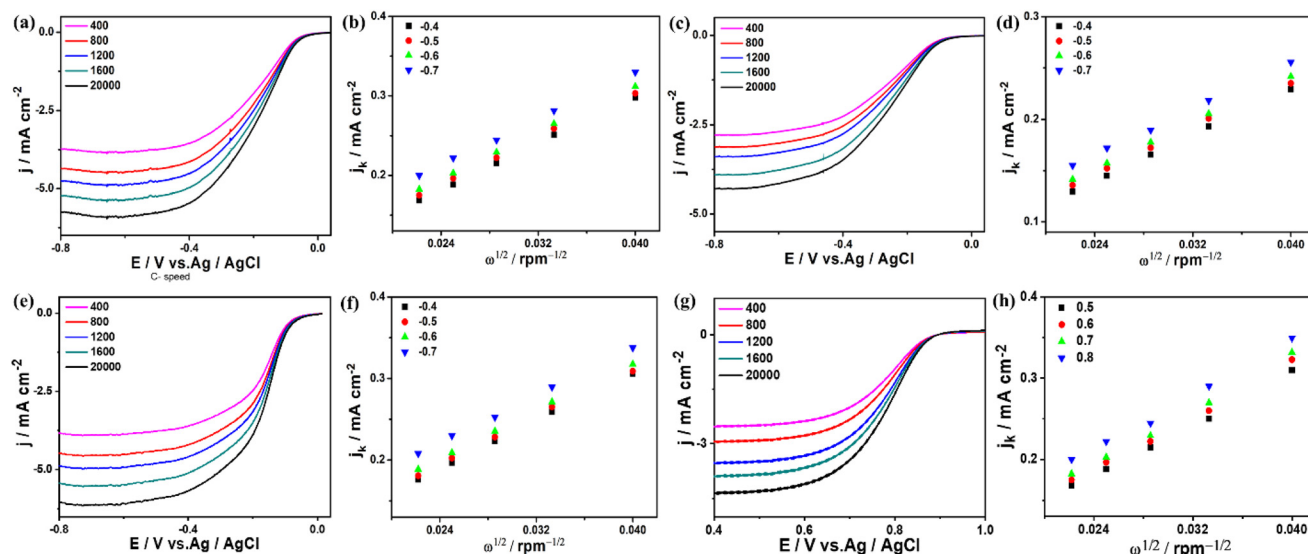
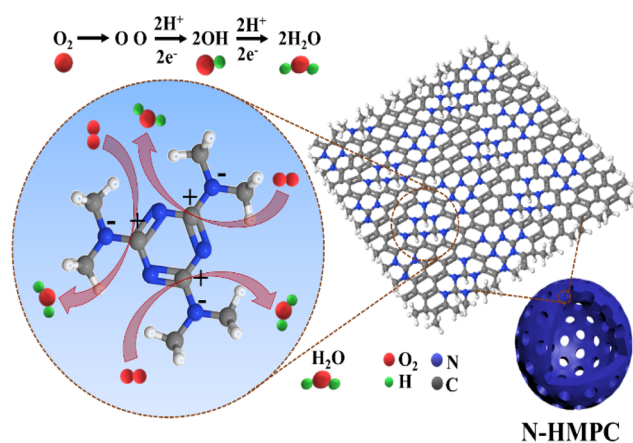


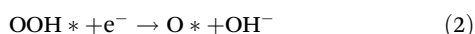
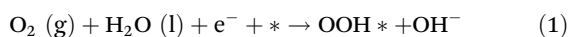
Fig. 7 RDE voltammograms for the ORR measured in O₂-saturated 0.1 M KOH solution at 20 mV s⁻¹ under various rotation speeds and their K-L plots at different electrode potentials for (a and b) N-HMPC, (c and d) HMPC, and (e-f) Pt/C. (g and h) RDE voltammograms for the ORR measured in O₂-saturated 0.5 M H₂SO₄ solution at 20 mV s⁻¹ under various rotation speeds and its K-L plots at different electrode potentials for N-HMPC.



Scheme 2 The proposed ORR mechanism on N-HMPC.

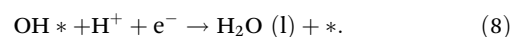
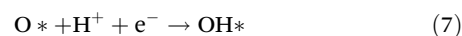
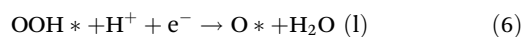
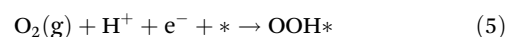
were performed according to the computational hydrogen electrode approach pioneered by Nørskov *et al.*^{54,55} Further details about the model construction and governing can be found in the ESI.† The free energy diagrams are calculated at zero electrode potential ($U = 0$) and the equilibrium potential ($U = 0.455$ V and 1.23 V for alkaline and acidic media, respectively). We have optimized the geometries of OOH*, O*, and OH* on the N-HMPC enriched with 25%.

In the alkaline medium, the four ORR elementary steps are summarized as:



where * refers to the adsorption site on the catalyst and OOH*, OH*, and O* are the adsorbed intermediates on the catalyst.

We have observed a spontaneous dissociation of O₂ on the N-HMPC and the formation of two O* sites (Fig. 8a) in KOH, indicating that the underline mechanism for this catalyst is the dissociative one similar to that on the Pt catalyst. Also, the optimization of OOH* leads to O* and OH* (Fig. 8b) in H₂SO₄, confirming the dissociative mechanism. The ORR dissociative mechanism involves a direct formation of O* followed by eqs (3) and (4). The ORR diagram of N-HMPC shows a spontaneous exothermic dissociation of O₂ into O*, while the formation of OH* and OH⁻ species are endothermic (Fig. 8c). This ORR profile is similar to that of the Pt catalyst, although they do not share the same energetics. The heat release from the first step is used to overcome the sluggish second and third steps. Indeed, at the equilibrium electrode potential ($U = 0.455$ V), the barriers of the last two steps are 1.06, and 1.40 eV, respectively, which could be overcome by the energy release of the first step (-3.86 eV).^{54,55} These results are in perfect agreement with our experimental findings on our developed N-HMPC catalyst. The elementary four steps of the ORR in the acidic medium are:



Regarding the dissociative mechanism in H₂SO₄ (eqs (5)–(8)), the N-HMPC has even more spontaneous dissociation of O₂ molecule into O* species (-7.87 and -10.33 eV at 0 and

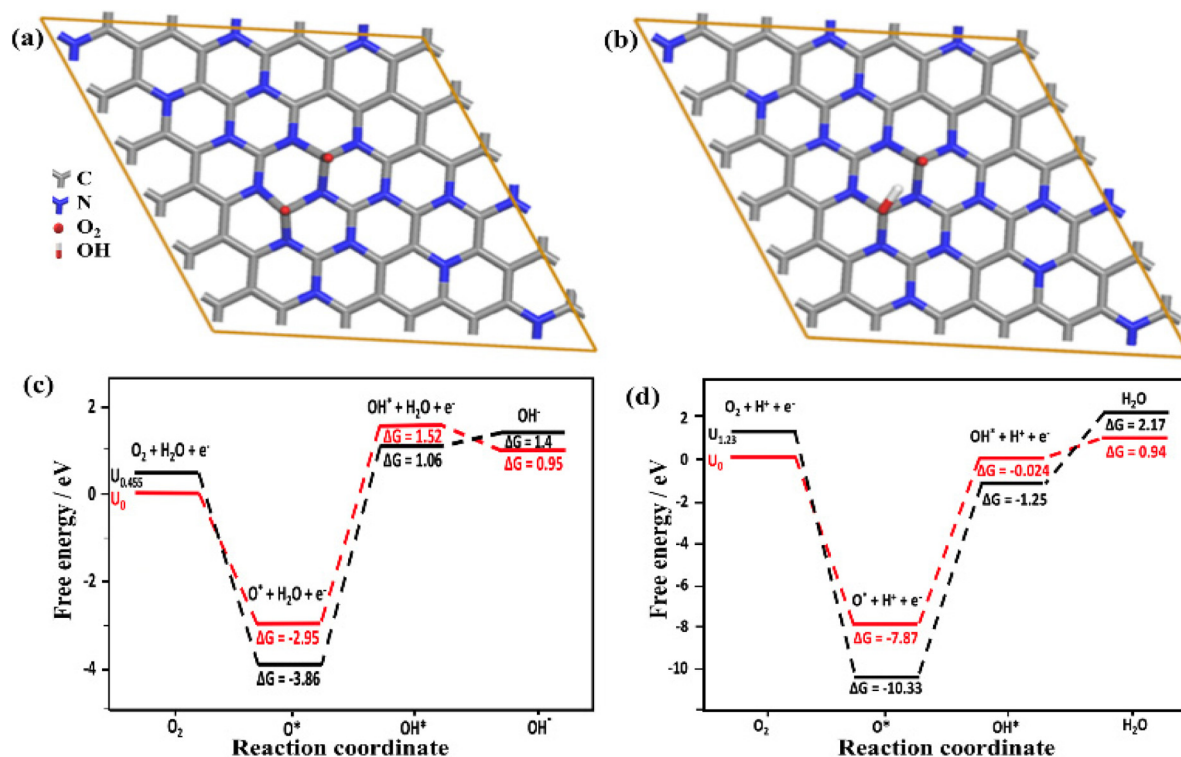


Fig. 8 The molecular models used in the periodic DFT simulations: (a) the optimized structure of O₂ on the N-HMPC sheet periodic in XY dimensions in alkaline media, which resulted in a spontaneous dissociation of O₂. (b) The optimized structure of OOH on N-HMPC also dissociated into OH* and O* species in acidic media. Free energy diagrams in alkaline (c) and acidic media (d) at zero and equilibrium potentials.

1.23 electrode potentials, respectively) (Fig. 8d). At $U = 0$, only the third step has a barrier of 0.94 eV, which is not difficult to surmount. Similarly, at $U = 1.23$ eV, the two early steps are exothermic, and only the last step has a barrier of 2.17 eV, which is manageable with the energy released from the first step.^{54,55} The barrier of the last step in KOH and H₂SO₄ media is in a good correlation with the experimental performance of our newly prepared N-HMPC. Indeed, our catalyst is performing better in the alkaline medium. Altogether, DFT simulations predict that the ORR mechanism is dissociative on the N-HMPC and highly exothermic in the first step, which consists of the O* formation.^{54,55} The energy released from the first step is used to surmount the following endothermic steps. This is very beneficial for N-HMPC because the first and the last steps are the main rate-determining steps for many reported materials in literature.^{54,55} The nitrogen in N-HMPC induced high polarization sites, which are favorable for the stabilization of the O₂ dissociation products (O*).

The presented results have demonstrated a high electrocatalytic aptitude of N-HMPC, competitively higher than that of commercial Pt/C in KOH, besides a cognitive activity in H₂SO₄. The origin of activity enhancement is owed to the hierarchical core-shell porous structure and nitrogen doping. Mainly, N-HMPC nanocapsules with enormous multiple pores and high surface area provided abundant catalytically active sites for ORR.^{35,42–45} Moreover, the nanocapsule morphology

with a thin porous graphitic-like carbon facilitated the adsorption of O₂ molecules, allowing for quick diffusion to the inner pores, which maximized the utilization of the inner surface during ORR.^{35,42–45} Oxygen can be activated by direct bonding to carbon atoms close to the N-doped sites, which resulted in polarization sites that enhanced the adsorption of the released O* species. This step is preceded by the promotion of the carbon π -electrons to the antibonding orbitals of O₂, activating O–O splitting under low potential.^{24,51–53} This resulted in the creation of additional catalytically active sites and accelerating ORR kinetics with a high tolerance to ORR poisoning species.

Conclusions

In summary, we have presented a facile green strategy for one-pot fabrication of graphitic-like sub-100 nm N-HMPC nanocapsules *via in situ* formation of a thin layer of resorcinol-melamine-formaldehyde enveloping a silica core followed by carbonization and eroding the silica core. This allowed the formation of sub-100 nm graphitic-like hollow carbon capsules enriched with nitrogen (25 wt%), outstanding surface area (790 m² g⁻¹), and multiple pores; N-content could be tuned by changing the melamine concentration. The ORR catalytic activity of N-HMPC nanocapsules is found to be closer to commercial Pt/C catalyst in KOH and H₂SO₄. Meanwhile, N-HMPC



was significantly more stable than Pt/C. The presented method can be applicable for tailoring the shape and composition of other carbon-based structures for deployment as efficient electrocatalysts for ORR and other electrocatalytic reactions. The proposed material provides a viable solution to replace scarce noble metal catalysts, at a dramatically lower cost, without compensating the activity or stability, which is believed to be a huge techno-economical boost to further commercializing the fuel cell technology.

Conflicts of interest

There are no conflicts to declare.

Acknowledgements

This work was supported by Gas Processing Center (GPC), College of Engineering, Qatar University, Doha 2713, Qatar. The authors thank King Abdullah University of Science & Technology (KAUST) for providing its computational resources (supercomputer Shaheen).

References

- 1 X. Wan, X. Liu, Y. Li, R. Yu, L. Zheng, W. Yan, H. Wang, M. Xu and J. Shui, *Nat. Catal.*, 2019, **2**, 259.
- 2 G. de Falco, M. Florent and T. J. Bandosz, *Green Chem.*, 2020, **22**, 7858–7870.
- 3 W. Wang, X. Li, T. He, Y. Liu and M. Jin, *Nano Lett.*, 2019, **19**, 1743–1748.
- 4 S.-I. Choi, M. Shao, N. Lu, A. Ruditskiy, H.-C. Peng, J. Park, S. Guerrero, J. Wang, M. J. Kim and Y. Xia, *ACS Nano*, 2014, **8**, 10363–10371.
- 5 X. Tong, J. Zhang, G. Zhang, Q. Wei, R. Chenitz, J. P. Claverie and S. Sun, *Chem. Mater.*, 2017, **29**, 9579–9587.
- 6 X. Zhao, S. Takao, K. Higashi, T. Kaneko, G. Samjeske, O. Sekizawa, T. Sakata, Y. Yoshida, T. Uruga and Y. Iwasawa, *ACS Catal.*, 2017, **7**, 4642–4654.
- 7 H. Wang, S. Yin, K. Eid, Y. Li, Y. Xu, X. Li, H. Xue and L. Wang, *ACS Sustainable Chem. Eng.*, 2018, **6**, 11768–11774.
- 8 A. Abdelhafiz, A. Vitale, C. Joiner, E. Vogel and F. M. Alamgir, *ACS Appl. Mater. Interfaces*, 2015, **7**, 6180–6188.
- 9 A. Abdelhafiz, A. Vitale, P. Buntin, B. deGlee, C. Joiner, A. Robertson, E. M. Vogel, J. Warner and F. M. Alamgir, *Energy Environ. Sci.*, 2018, **11**, 1610–1616.
- 10 L. Lv, D. Zha, Y. Ruan, Z. Li, X. Ao, J. Zheng, J. Jiang, H. M. Chen, W.-H. Chiang, J. Chen and C. Wang, *ACS Nano*, 2018, **12**, 3042–3051.
- 11 Y. Zheng, Y. Jiao, M. Jaroniec, Y. G. Jin and S. Z. Qiao, *Small*, 2012, **8**, 3550–3566.
- 12 A. A. Gewirth, J. A. Varnell and A. M. DiAscro, *Chem. Rev.*, 2018, **118**, 2313–2339.
- 13 L. F. Wu, H. B. Feng, M. J. Liu, K. X. Zhang and J. H. Li, *Nanoscale*, 2013, **5**, 10839–10843.
- 14 X. Yan, Y. Jia and X. Yao, *Chem. Soc. Rev.*, 2018, **47**, 7628–7658.
- 15 H. B. Wang, T. Maiyalagan and X. Wang, *ACS Catal.*, 2012, **2**, 781–794.
- 16 C. Wei, H. Wang, K. Eid, J. Kim, J. H. Kim, Z. A. Allothman, Y. Yamauchi and L. Wang, *Chem. – Eur. J.*, 2017, **23**, 637–643.
- 17 M. A. Ahsan, M. A. Imam, A. R. P. Santiago, A. Rodriguez, B. Alvarado-Tenorio, R. Bernal, R. Luque and J. C. Noveron, *Green Chem.*, 2020, **22**, 6967–6980.
- 18 K. Gong, F. Du, Z. Xia, M. Durstock and L. Dai, *Science*, 2009, **323**, 760–764.
- 19 J. Masa, W. Xia, M. Muhler and W. Schuhmann, *Angew. Chem., Int. Ed.*, 2015, **54**, 10102–10120.
- 20 H.-W. Liang, X. Zhuang, S. Brüller, X. Feng and K. Müllen, *Nat. Commun.*, 2014, **5**, 1–7.
- 21 Q. Lv, W. Si, J. He, L. Sun, C. Zhang, N. Wang, Z. Yang, X. Li, X. Wang and W. Deng, *Nat. Commun.*, 2018, **9**, 1–11.
- 22 S. Chen, J. Bi, Y. Zhao, L. Yang, C. Zhang, Y. Ma, Q. Wu, X. Wang and Z. Hu, *Adv. Mater.*, 2012, **24**, 5593–5597.
- 23 H. Yu, L. Shang, T. Bian, R. Shi, G. I. Waterhouse, Y. Zhao, C. Zhou, L. Z. Wu, C. H. Tung and T. Zhang, *Adv. Mater.*, 2016, **28**, 5080–5086.
- 24 P. Chen, L.-K. Wang, G. Wang, M.-R. Gao, J. Ge, W.-J. Yuan, Y.-H. Shen, A.-J. Xie and S.-H. Yu, *Energy Environ. Sci.*, 2014, **7**, 4095–4103.
- 25 S. Zhang, Q. Chen and X. Li, *Green Chem.*, 2021, **23**, 6898–6925.
- 26 S.-A. Wohlgemuth, R. J. White, M.-G. Willinger, M.-M. Titirici and M. Antonietti, *Green Chem.*, 2012, **14**, 1515–1523.
- 27 N. Brun, S. A. Wohlgemuth, P. Osiceanu and M. M. Titirici, *Green Chem.*, 2013, **15**, 2514–2524.
- 28 M. Wu, J. Qiao, K. Li, X. Zhou, Y. Liu and J. Zhang, *Green Chem.*, 2016, **18**, 2699–2709.
- 29 S. A. Nicolae, H. Au, P. Modugno, H. Luo, A. E. Szego, M. Qiao, L. Li, W. Yin, H. J. Heeres and N. Berge, *Green Chem.*, 2020, **22**, 4747–4800.
- 30 K. Eid, M. H. Sliem and A. M. Abdullah, *Nanoscale*, 2019, **11**, 11755–11764.
- 31 X. Ning, Y. Li, J. Ming, Q. Wang, H. Wang, Y. Cao, F. Peng, Y. Yang and H. Yu, *Chem. Sci.*, 2019, **10**, 1589–1596.
- 32 S. A. Shaik, S. Sengupta, R. S. Varma, M. B. Gawande and A. Goswami, *ACS Sustainable Chem. Eng.*, 2021, **9**, 3–49.
- 33 K. Eid, M. H. Sliem, H. Al-Kandari, M. A. Sharaf and A. M. Abdullah, *Langmuir*, 2019, **35**, 3421–3431.
- 34 C. Zhu, M. Takata, Y. Aoki and H. Habazaki, *Chem. Eng. J.*, 2018, **350**, 278–289.
- 35 L. J. Zhang, Z. X. Su, F. L. Jiang, L. L. Yang, J. J. Qian, Y. F. Zhou, W. M. Li and M. C. Hong, *Nanoscale*, 2014, **6**, 6590–6602.



- 36 Y. Fang, Y. Y. Lv, R. C. Che, H. Y. Wu, X. H. Zhang, D. Gu, G. F. Zheng and D. Y. Zhao, *J. Am. Chem. Soc.*, 2013, **135**, 1524–1530.
- 37 H. Jin, H. M. Zhang, H. X. Zhong and J. L. Zhang, *Energy Environ. Sci.*, 2011, **4**, 3389–3394.
- 38 P. Chen, T. Y. Xiao, Y. H. Qian, S. S. Li and S. H. Yu, *Adv. Mater.*, 2013, **25**, 3192–3196.
- 39 L. S. Panchalkarla, A. Govindaraj and C. N. R. Rao, *ACS Nano*, 2007, **1**, 494–500.
- 40 S. Feng, W. Li, Q. Shi, Y. Li, J. Chen, Y. Ling, A. M. Asiri and D. Zhao, *Chem. Commun.*, 2014, **50**, 329–331.
- 41 X. Liu, S. Li, J. Mei, W.-M. Lau, R. Mi, Y. Li, H. Liu and L. Liu, *J. Mater. Chem. A*, 2014, **2**, 14429–14438.
- 42 A. Zhao, J. Masa, W. Schuhmann and W. Xia, *J. Phys. Chem. C*, 2013, **117**, 24283–24291.
- 43 K. Parvez, S. Yang, Y. Hernandez, A. Winter, A. Turchanin, X. Feng and K. Müllen, *ACS Nano*, 2012, **6**, 9541–9550.
- 44 N. López-Salas, M. C. Gutiérrez, C. O. Ania, M. A. Muñoz-Márquez, M. Luisa Ferrer and F. D. Monte, *J. Mater. Chem. A*, 2016, **4**, 478–488.
- 45 X. Zhao, X. Zou, X. Yan, C. L. Brown, Z. Chen, G. Zhu and X. Yao, *Inorg. Chem. Front.*, 2016, **3**, 417–421.
- 46 S. Lu, K. Eid, Y. Deng, J. Guo, L. Wang, H. Wang and H. Gu, *J. Mater. Chem. A*, 2017, **5**, 9107–9112.
- 47 K. Eid, H. Wang, V. Malgras, Z. A. Allothman, Y. Yamauchi and L. Wang, *J. Phys. Chem. C*, 2015, **119**, 19947–19953.
- 48 J. Zhang, Z. Zhao, Z. Xia and L. Dai, *Nat. Nanotechnol.*, 2015, **10**, 444.
- 49 L. Lai, J. R. Potts, D. Zhan, L. Wang, C. K. Poh, C. Tang, H. Gong, Z. Shen, J. Lin and R. S. Ruoff, *Energy Environ. Sci.*, 2012, **5**, 7936–7942.
- 50 S. Gao, X. Wei, H. Liu, K. Geng, H. Wang, H. Moehwald and D. Shchukin, *J. Mater. Chem. A*, 2015, **3**, 23376–23384.
- 51 K. Wan, Z. P. Yu, X. H. Li, M. Y. Liu, G. Yang, J. H. Piao and Z. X. Liang, *ACS Catal.*, 2015, **5**, 4325–4332.
- 52 Q. Lv, W. Y. Si, J. J. He, L. Sun, C. F. Zhang, N. Wang, Z. Yang, X. D. Li, X. Wang, W. Q. Deng, Y. Z. Long, C. S. Huang and Y. L. Li, *Nat. Commun.*, 2018, **9**, 11.
- 53 T. Najam, S. S. A. Shah, W. Ding, J. X. Jiang, L. Jia, W. Yao, L. Li and Z. D. Wei, *Angew. Chem., Int. Ed.*, 2018, **57**, 15101–15106.
- 54 R. Ma, G. Lin, Y. Zhou, Q. Liu, T. Zhang, G. Shan, M. Yang and J. Wang, *npj Comput. Mater.*, 2019, **5**, 1–15.
- 55 J. K. Nørskov, F. Abild-Pedersen, F. Studt and T. Bligaard, *Proc. Natl. Acad. Sci. U. S. A.*, 2011, **108**, 937–943.

